Asian Journal of Chemistry; Vol. 33, No. 8 (2021), 1941-1949

ASIAN JOURNAL OF CHEMISTRY

https://doi.org/10.14233/ajchem.2021.23244

One-Pot Synthesis of Pt-Pd Nanospheres Anchored in 2D-Reduced Graphene Oxide Sheets for Electrocatalytic Methanol Oxidation

G. Sreenivasa Kumar, N. Ramamanohar Reddy, B. Vijaya Kumar Naidu and S. Adinarayana Reddy*

Department of Materials Science and Nanotechnology, Yogi Vemana University, Kadapa-516005, India

*Corresponding author: E-mail: anreddyphd@gmail.com

Received: 11 April 2021; *Accepted*: 15 July 2021; *Published online*: 26 July 2021; AJC-20450

Recently, direct methanol fuel cells (DMFCs) have been identified as suitable alternatives for efficient energy conversion and pollution-free technology. This study reports the preparation of binary platinum-palladium (Pt-Pd) nanospheres anchored on reduced graphene oxide (rGO) sheets (Pt-Pd/rGO sheets) using a wet chemical technique. The structural and morphological features were analyzed using X-ray powder diffraction (XRD), scanning electron microscopy (SEM), transmission electron microscopy (TEM), Raman microscope and Fourier transform infrared (FTIR) spectroscopy. The homogeneous anchored Pt-Pd nanospheres with an average size of 3.85 nm were deposited on to the surface of rGO sheets. Methanol oxidation studies were analyzed through a simple drop coating method using a glassy carbon electrode (GCE). The methanol oxidation performance of the Pt-Pd/rGO nanospheres coated GCE was higher than that of the rGO sheets coated with a single metal (Pt or Pd). The concordant integration of the Pt and Pd nanospheres/rGO-interface improved performance.

Keywords: Bimetallic Pt-Pd nanospheres, rGO sheets, Electrocatalyst, Methanol electro-oxidation.

INTRODUCTION

Recently, the energy demand and energy crisis have gained widespread interest because most modern energy systems use fossil fuels, which are unsustainable over the long-term [1,2]. Efforts are being made to diversify clean and new energy sources to allow for cleaner and more readily available energy sources. Direct methanol fuel cells (DMFCs) have the potential to become the new green energy resources for various mobile and stationary applications. DMFCs have greater energy conversion efficiency and allow for a more eco-friendly operation [3,4]. A significant amount of research has been conducted on developing promising electrocatalysts, proton exchange membranes and gas flow fields. However, there are still several challenges that have to be addressed, such as the poisoning effect of intermediate species formed during oxygen reduction reaction (ORR) or methanol oxidation reaction (MOR), insufficient durability and fuel crossover [5] when implemented in day-to-day life (commercial applications). Consequently, it is crucial to develop novel and durable electrocatalyst configurations with sufficient electrocatalytic activity for MOR and ORR [6-9]. Platinum is a well-known metal used for methanol dissociative adsorption. However, the carbon monoxide generated during methanol oxidation contaminates the strong platinum surface, which decelerates its catalytic performance [10-13]. Therefore, extensive research has been conducted to combine Pt with other metals (*i.e.*, ruthenium, palladium, gold and silver) to form Pt-based alloys. These alloys (*i.e.*, PtRu, Pt-Pd, PtAu and PtAg) that have various morphologies, surface modifications and composite materials decrease the cost and alter the tolerance of the self-contamination property of Pt [14-20]. The Pt-Pd alloy improves the catalytic performance of Pt because Pd has a similar catalytic performance as compared to that of Pt, is cheaper than Pt and can reduce the contamination effect of Pt by weakening the Pt-CO_{ads} bonds.

Two dimensional (2D) categories of reduced graphene oxide (rGO) sheets are broadly studied in physics and material sciences for carbonaceous materials. The rGO sheets can act as supporting material on which metal nanoparticles can be placed for DMFC applications because the rGO sheets have superior electrical conductivity, chemical inertness and surface area. Furthermore, the organic functional groups [*i.e.* epoxy (C–O–C), carboxyl (–COOH), carbonyls (–CO) and hydroxyl (–OH)] which are present in the rGO sheets act as anchoring

groups for metal ion interactions in the liquid phase and facilitate well-dispersed metal deposits over the rGO sheets [21-23]. Yang *et al*. [24] synthesized Pt-Pd bimetallic nanoparticles supported on graphene nanosheets through a hydrothermal method using P123 copolymer as a reducing agent and stabilizer for the methanol oxidation. Other researchers [25-27] reported dendritic hybrid Pt-Pd NPs on rGO sheets through sonication using F127 and ascorbic acid as a surfactant and reducing agent, respectively. They achieved a high electrochemical activity for MOR. Feng *et al.* [28] reported Pt@Pd/rGO core shell structure nanoparticles showed better MOR activity than Pt/rGO and Pd/rGO materials. Zhang *et al.* [29] reported the bimetallic alloyed $Pt_{71}CO_{29}$ material exhibited better MOR and ORR activity than the commercial Pt black. These results suggested that rGO sheets can act as supporting materials and as an ideal substrate for anchoring and growing Pt-Pd bimetallic nanoparticles to create high performing electrocatalysts for MOR.

This study investigates the feasibility of a wet chemical reduction method toward the fabrication of well-dispersed Pt-Pd nanospheres on a rGO support sheet. The prepared Pt-Pd nanospheres/rGO sheets demonstrated promising catalytic activity toward methanol electrooxidation when compared to the similarly prepared Pt/rGO and Pd/rGO NSs because of the concordant integration between Pt and Pd and the positive contribution of the rGO. Generally, this fabrication strategy can also be used to prepare other bimetallic or trimetallic configurations with controlled structures and catalytic activities.

EXPERIMENTAL

Preparation of graphene oxide: In a typical synthesis, 5 g of pure graphite powder was first dispersed in 115 mL of conc. H_2SO_4 in a 1000 mL beaker under ice bath with magnetic stirring and 15 g of potassium permanganate slowly into the mixture under ice bath with continuous stirring for 40 min and 2.5 g of sodium nitrate was added and kept it for 1 h. Subsequently, the beaker was removed from the ice bath and keep at room temperature under continuous stirring for 1 h. The resultant solution was heated on a water bath at 35 ºC for 30 min under continuous stirring and then 800 mL of distilled water was added slowly and raised the temperature to 98 ºC for 15 min under vigorous stirring and then cooled to room temperature. Finally, 30 mL of H_2O_2 was added to remove the excess $KMnO_4$ residues. The product was washed first with 1 M of HCl and followed by washing with double distilled water repeatedly until the pH of the product reaches neutrality. The final product was centrifuged and dried at 60 ºC in a vacuum oven for 8 h.

Preparation of electrocatalysts: All the chemicals that were used in this study are of analytical grade and use as such. Graphene oxide was prepared using natural graphite flakes through a modified Hummer's method [30]. Bimetallic Pt-Pd NSs/rGO nanospheres were prepared using a wet chemical reflux method. First, 20 mg of synthesized graphite oxide (20 %) was suspended in 20 mL of distilled water and sonicated for 1 h. Then, 25 mL of 0.01 M of Na_2PdCl_4 (50 %) and 25 mL of 0.01 M of $H_2PtCl_6 \cdot 6H_2O$ (30 %) were added to the suspension while stirring. The pH of the reaction was maintained at 12 by adding 1 M of NaOH. Furthermore, 30 mL of freshly prepared 1 M ascorbic acid was added dropwise. The resulting solution was refluxed at 95 ºC for 6 h to allow simultaneous reduction of Pd^{2+}, Pt^{4+} and graphene oxide (GO), creating Pt-Pd/rGO nanospheres. The precipitate was collected and washed several times using ethanol and distilled water. The final Pt-Pd/rGO nanospheres was centrifuged and dried in a hot air oven at 80 ºC for 6 h. A similar process was used to fabricate Pt/rGO and Pd/rGO nanospheres for comparison purposes. **Scheme-I** shows the preparation procedure adapted for the electrocatalysts used in this study.

Electrochemical measurements: The electrochemical measurements of the synthesized electrocatalysts were recorded using a CHI potentiostat (model CH Instruments 6002 E, USA) equipped with standard electrochemical cells (Pt and silver/silver chloride (Ag/AgCl) and saturated KCl as an auxiliary electrode and reference electrode, respectively) and a 0.5 M H_2SO_4 + 1 M CH_3OH solution as the electrolyte. The catalyst slurry was prepared using 2 mg of as-synthesized catalyst in a mixed solvent solution (700 µL of deionized water, 800 µL of ethanol and 1000 µL of 0.5 wt.% of Nafion) and was ultrasoni-

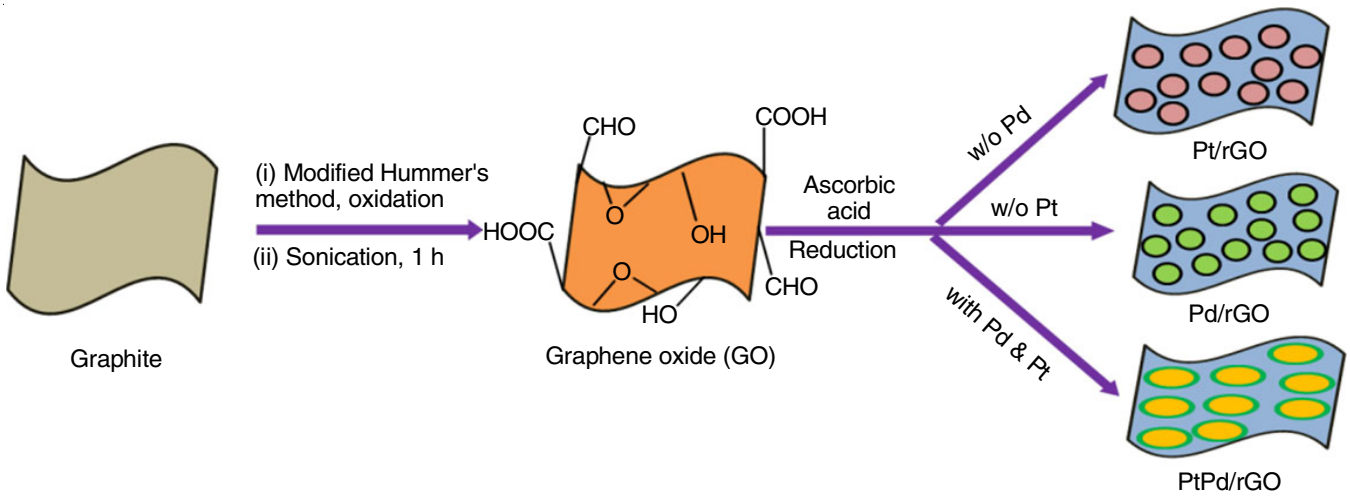

Scheme-I: Schematic illustration of rGO-supported metallic (Pt, Pd and Pt-Pd) nanospheres

cated for 30 min. The working electrode was prepared by dropping 5 µL of the catalyst slurry onto the polished glassy carbon electrode (GCE) surface using a micropipette and it was then air-dried in ambient conditions. The electrochemical surface area (ECSA) of the synthesized materials was measured using stable cyclic voltammograms (CV).

Physical characterization: The crystalline nature of electro-catalysts was primarily confirmed by powder X-ray diffraction (Bruker D8, Germany) using a Cu*K*α radiation of 1.545 Å wavelength. Structural defects of rGO-based materials were recorded by Raman spectroscopy using WiTec alpha 200 SNOM, Germany. Functional group information of GO, rGO, rGO-supported catalysts were obtained by Fourier transformed infrared spectroscopy using a Perkin-Elmer spectrum Two™ spectrometer in the range from 4000-500 cm^{-1}. The morphology and structural features of the samples were evaluated using FE-SEM (Carl Zeiss, Germany) and TEM (JEM 3010-JEOL) analysis. Elemental analysis was performed with a field emission scanning electron microscope equipped with an EDS detector (Oxford Instruments). X-ray photoelectron spectra (XPS) were recorded using a KRATOS AXIS 165 (Canada) photoelectron spectrometer operated with Mg-Kα energy radiation.

RESULTS AND DISCUSSION

XRD studies: The crystalline features of the prepared materials were studied using X-ray powder diffraction (XRD) patterns shown in Fig. 1. The Braggs peak appeared at 2θ = 23.92º on the (002) plane of the rGO. The diffraction features of the synthesized Pt/rGO and Pd/rGO are well-matched with the face-centered cubic Pt (JCPDS card no. 04-0802) and Pd (JCPDS card no. 46-1043), respectively [31,32]. The Braggs planes of Pt-Pd NSs/rGO NSs were observed at 2θ = 39.94º, 46.18º and 67.62º, which can be indexed to the (111), (200) and (220) planes, respectively. A slight shift in the diffraction planes of Pt-Pd NSs/rGO produced higher Bragg angles when compared with the relative fcc-Pt reflections diffraction peaks.

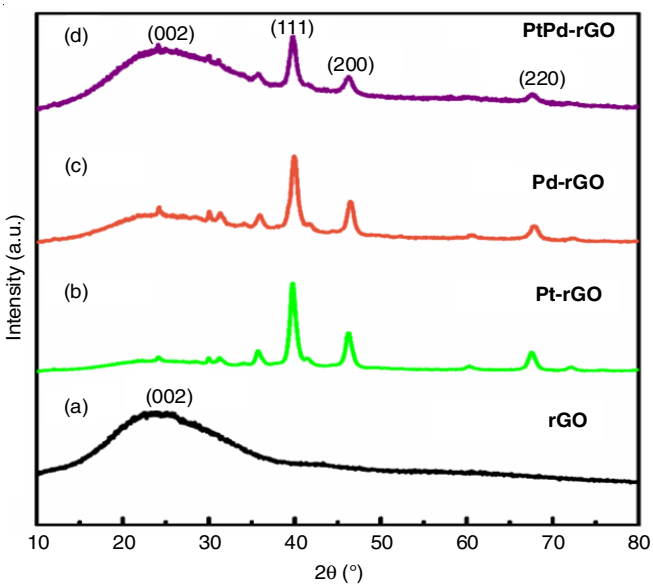

Fig. 1. Powder XRD patterns of rGO and rGO-based metallic (Pt, Pd and Pt-Pd) nanospheres

This indicated that a certain degree of alloying between Pt and Pd occurred [33]. The crystallite size, calculated in the (111) Bragg plane of the Pt-Pd/rGO, was approximately 3.85 nm and aligned with the transmission electron microscopy (TEM) analysis. The appearance of intense XRD patterns suggests that the produced electrocatalysts have a high degree of crystallinity.

Raman spectra: Raman spectroscopy is an essential tool for evaluating the graphitic degree of the rGO sheets subsequent to the deposition of metallic particles (*i.e.*, Pt, Pd and Pt-Pd). The corresponding Raman spectral features are shown in Fig. 2. The D and G band pairs of the GO and rGO were 1348 and 1597 cm^{-1} and 1348 and 1598 cm^{-1}, respectively. The intensity ratio of D to G (I_D/I_G) was used to assess the reduction of the GO and deposition of the metallic particles on the rGO [34]. The D and G band values of the samples are centered at 1337 and 1598 cm^{-1}, respectively. The deviation of the I_D/I_G ratio indicates that the Pt, Pd and Pt-Pd has a significant effect on the graphite degree of the rGO sheets [35]. The appearance of small scale in-plane sp^2 domains in the composites is evidenced by the high magnitude of I_D/I_G ratios. This substantiates the presence of the few-layered rGO in metal/rGO composites. This is critical for achieving improved electrochemical activity in the nanohybrid composites.

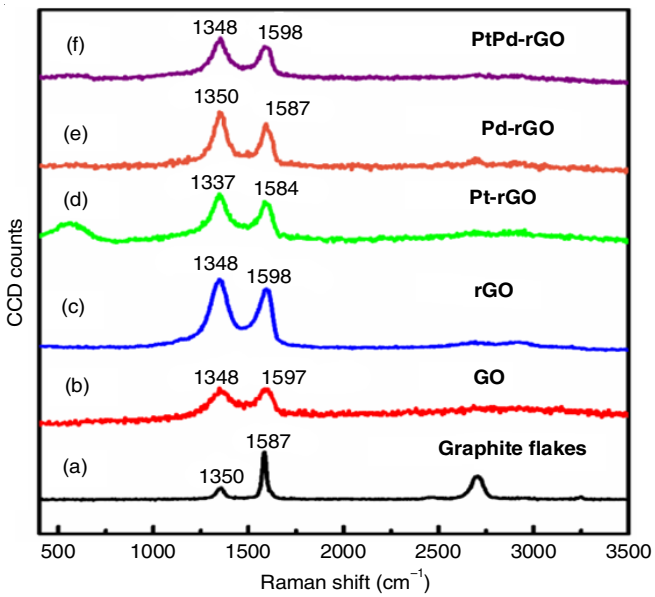

Fig. 2. Raman spectra of graphite, GO, rGO and rGO-based metallic (Pt, Pd and Pt-Pd)

FTIR spectra: During the chemical reduction method, Fourier transform infrared (FTIR) spectroscopy was used to examine the functional groups of the rGO sheets after the deposition of the metallic particles. The FTIR spectra (Fig. 3) of GO showed absorption peaks centered at 3438 and 1736 cm^{-1} representing the OH and C=O stretching modes, respectively. Furthermore, the absorption peaks located at 1384, 1260 and 1020 cm^{-1} corresponded to the OH located in the –COOH group. The bands that were located at 1626 and 2925 cm^{-1} show the unoxidized graphitic fields and stretching vibration of the C–H bonds. Furthermore, the intensity of the peaks that appeared at 1384 and 3443 cm^{-1} could indicate OH groups, respectively.

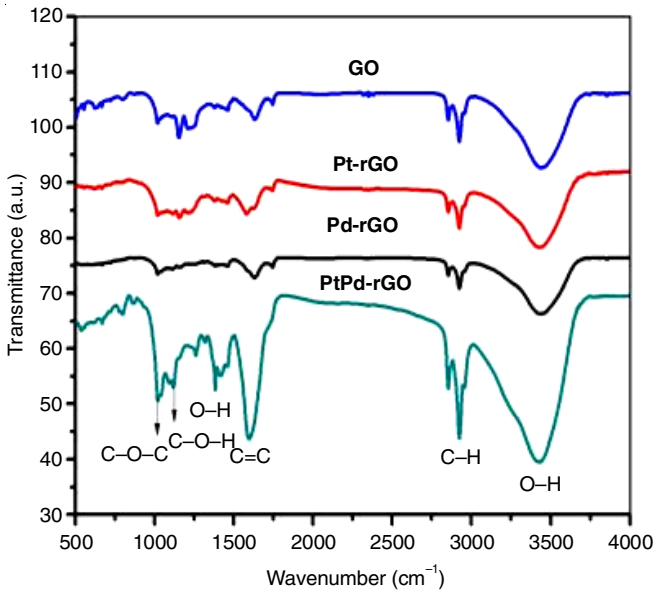

Fig. 3. FTIR spectra of GO and rGO-based metallic (Pt, Pd and Pt-Pd) nanospheres

These peaks were diminished, demonstrating a significant degree of GO reduction to rGO.

XPS spectra: The XPS spectrum analysis of the composites is shown in Fig. 4a. The peaks that appeared at binding energies of 71.50, 284.76, 336.38 and 532.25 eV could be attributed to Pt 4*f*, C 1*s*, Pd 3*d* and O 1*s*, respectively. This verifies the presence of Pt, Pd, C and O of the rGO in the nanocomposite and corresponds to the energy dispersive spectroscopy (EDS) data. The peak located at 284.8 eV is related to the C 1*s* peak of C-C bonds, substantiating the reduction of GO to rGO as shown in Fig. 4b. The XPS spectrum of Pt 4*f* in Fig. 4c shows two strong Pt^0 state peaks that relate to Pt $4f_{5/2}$ and Pt $4f_{7/2,}$ located at 74.4 and 71.4 eV, respectively. Further-more, the high-resolution spectrum of Pd 3*d* in Fig. 4d shows two strong Pd^0 peaks that relate to Pd $3d_{3/2}$ and Pd $3d_{5/2}$, located at 340.5 eV and 336.4 eV, respectively [20]. The majority of the Pt and Pd cations are reduced to Pt and Pd metal through ascorbic acid.

FESEM studies: FESEM shows the surface morphology of GO, Pt/rGO, Pd/rGO and Pt–Pd/rGO catalysts (Fig. 5). GO

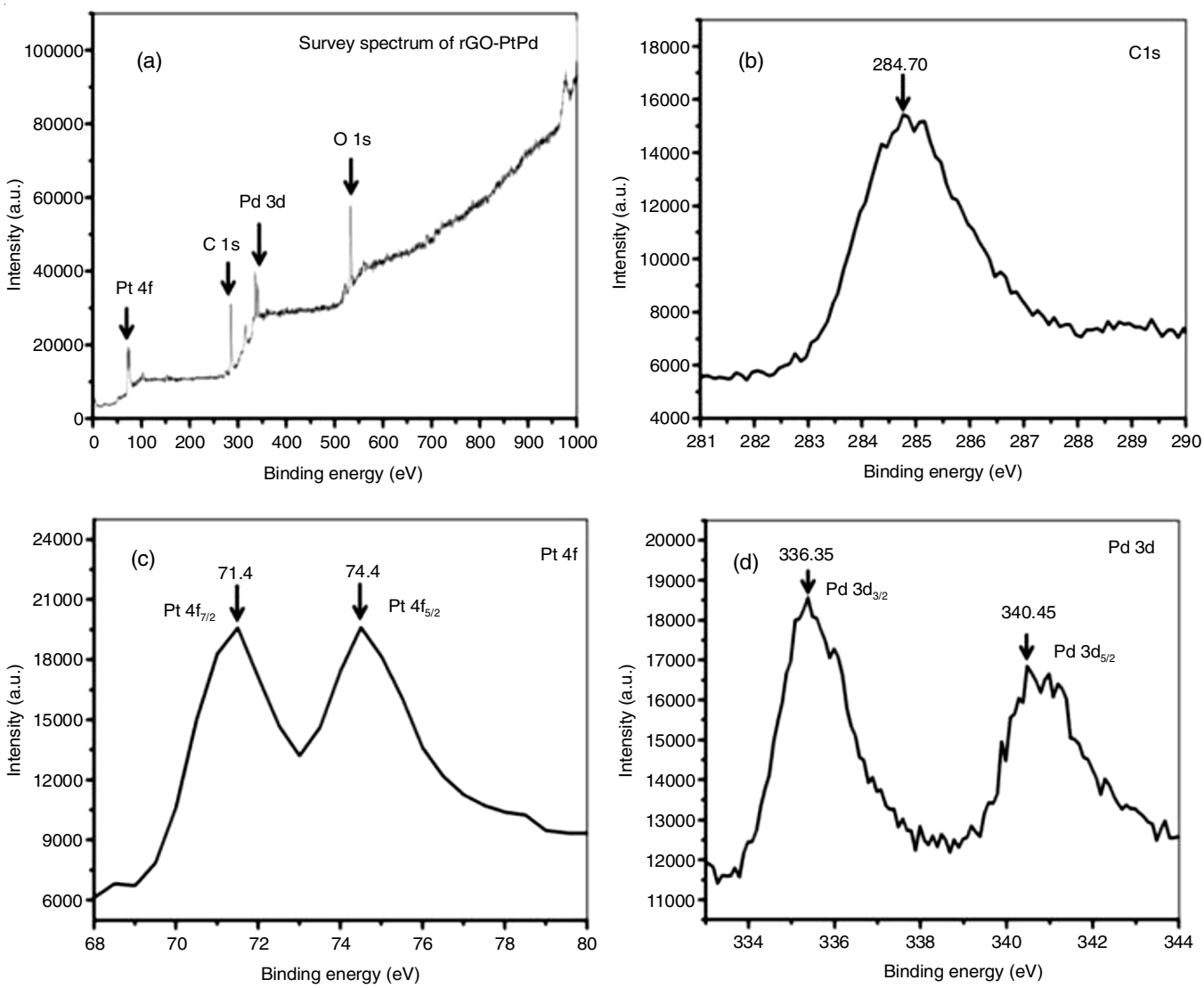

Fig. 4. XPS analysis of Pt-Pd/rGO electrocatalyst; (a) survey scan; (b) C1s XPS; (c) Pt 4f XPS; and (d) Pd 3d XPS

has sheet-like morphology as shown in Fig. 5a. Monometallic Pt, Pd and bimetallic Pt-Pd have spherical shapes and are densely deposited on the rGO sheets (Fig. 5b-d). These results confirm that the metallic nanospheres supported on rGO sheets will improve the electrocatalytic activity.

Fig. 6 shows the EDS profiles and quantitative analysis (insert) of the electrocatalysts and GO. Fig. 6a shows the elemental analysis of the GO. The GO contains carbon (C = 73 wt.%) and oxygen (O = 27 wt.%), which confirms that the natural graphite was converted to GO through an oxidation method. Fig. 6b shows EDS of the Pt/rGO, which contains platinum (Pt = 22 wt.%), carbon (C = 68 wt.%) and oxygen (O = 15 wt.%) owing to the introduction of Pt into the rGO sheets. Fig. 6c shows the Pd/rGO analysis spectra, which contains palladium (Pd = 35 wt.%), carbon (C = 40 wt.%) and oxygen (O = 25 wt.%). This confirms that the catalyst only contains these elements. Finally, Fig. 6d shows the elemental analysis of the Pt-Pd/rGO catalyst, which contains platinum (Pt = 40 wt.%), palladium (Pd = 34 wt.%), carbon (C = 18 wt.%) and oxygen (O = 7 wt.%).

TEM studies: The TEM images of different magnification ranges of the Pt-Pd/rGO nanocomposite is shown in Fig. 7. The images display several spherical particles which are well-dispersed on the rGO sheets. The EDS and XPS analysis indicate that these particles are bimetallic Pt-Pd nanospheres. The bimetallic Pt-Pd nanospheres are mainly 3-5 nm in size. The bimetallic Pt-Pd particle size, shape and uniformity of the coating on rGO sheets primarily influence electrocatalytic performance.

HRTEM studies: High-resolution transmission electron microscopy (HRTEM) analysis was used to investigate the crystalline and composite nature of the catalyst. Fig. 8 displays the HRTEM and selected area electron diffraction (SAED) pattern of the hybrid Pt-Pd NSs coated on the rGO sheets. The

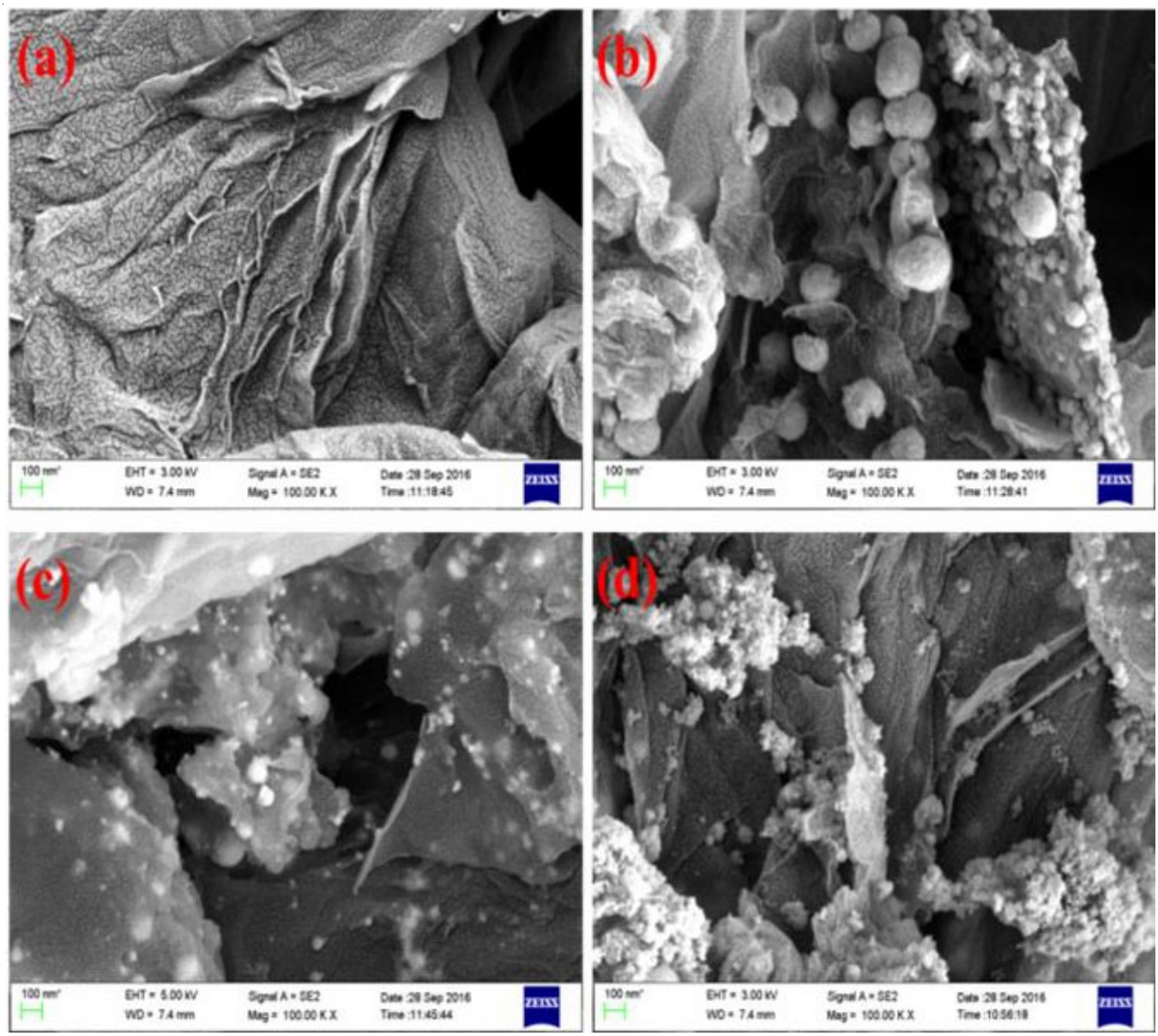

Fig. 5. SEM images of (a) GO; (b) Pt/rGO; (c) Pd/rGO; and (d) Pt-Pd/rGO nanospheres

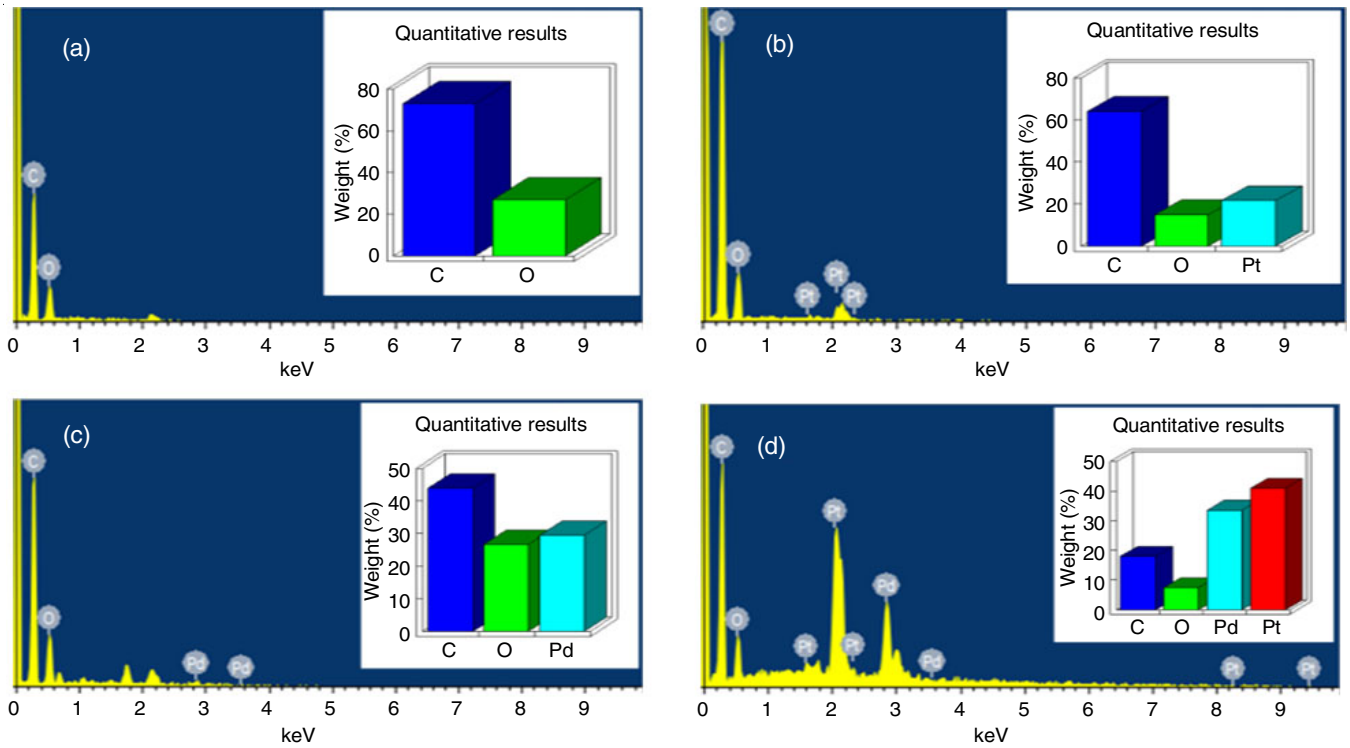

Fig. 6. EDS analysis of (a) GO; (b) Pt/rGO; (c) Pd/rGO; and (d) Pt-Pd/rGO nanospheres (insert: quantitative results)

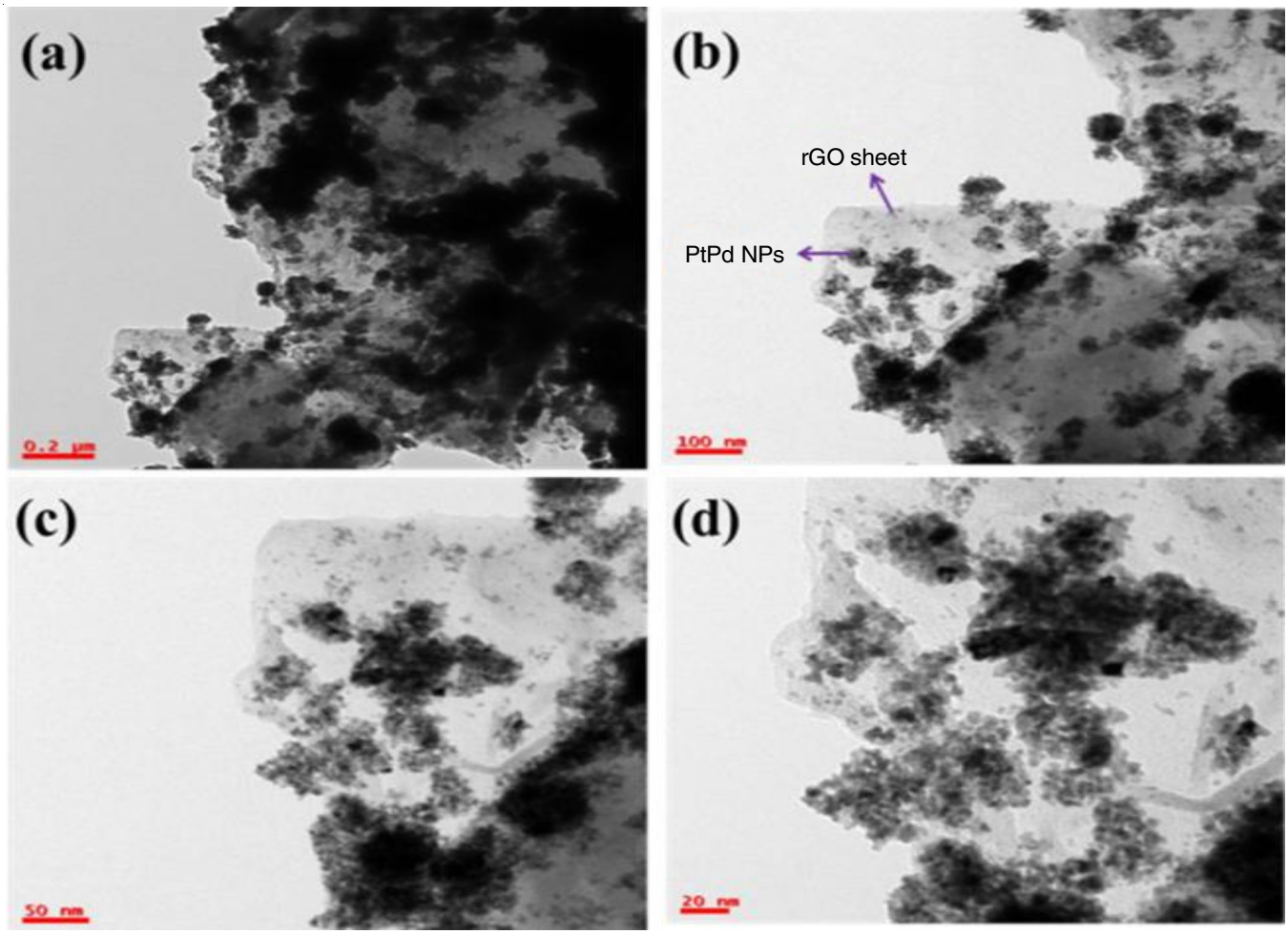

Fig. 7. TEM micrographs of bimetallic Pt-Pd/rGO nanospheres at various magnifications

rGO sheet demonstrated a single crystalline structure that had a wrinkled shape and a lattice spacing of 0.34 nm (Fig. 8a). The average diameter of the spherical-like Pt-Pd NP in Fig. 8b was 5 nm and a lattice spacing of 0.23 nm. Additionally, advantageous crystalline behaviour was shown by the SAED pattern. The sufficient thickness of the Pt-Pd nanosphere on rGO is crucial for the electrochemical activity of synthesized materials (Fig. 8d).

Electrochemical studies: The electrochemical performance of the metals supported by the rGO catalysts in the presence of a nitrogen atmosphere and a fresh 0.5 M H_2SO_4 solution was investigated using CV potential cycling. The CV experiment was performed by sweeping the electrode potential from -0.2 to 1.2 V *vs.* Ag/AgCl (saturated KCl) with a scan rate of 50 mV s^{-1} as shown in Fig. 9. Generally, the Pt-based catalyst electrode CV curve consists of two sections: the first section is the oxidation/reduction of Pt (0.8 - 1.2V) and the second section is the absorption/desorption of hydrogen (-0.2 to 0.1 V). The ionic adsorption takes place over the entire potential range (*i.e.* double layer capacitive behaviour in the rGO sheets). The electrochemical active surface area (ECSA) values of the Pt/C, Pd/rGO, Pt/rGO and Pt–Pd/rGO were 55.05, 58.48, 62.85 and 68.13 $m^2 g^{-1}$, respectively. The Pt–Pd/rGO catalyst showed a higher ECSA value when compared to the single metal-based rGO sheets owing to sufficient alloying and dispersion of nanospheres on the rGO sheets. Furthermore, these results indicate that the Pt-Pd/rGO catalyst delivers the highest number of active sites for the electrochemical adsorption/absorption of H-atoms onto or into the catalyst particle, respectively.

The methanol oxidation on the bimetallic Pt-Pd catalyst and single metals (*i.e.* Pt and Pd) in a 0.5 M H_2SO_4 + 1 M CH_3OH solution was examined using CV measurements at a 50 mV s^{-1} scan rate as shown in Fig. 10. Methanol adsorption was identified between 0.4 and 0.8 V when using freshly primed oxidation of chemisorbed species. The Faradic oxidation peaks of the carbonaceous species were detected at 0.6 V during the backward scan and detected on the Pt and Pd surface in the forward scan. The MOR of the Pt-Pd/rGO, Pt/rGO, Pt/C and Pd/rGO represented specific electro-oxidation of methanol was calculated as 0.31, 0.23, 0.1 and 0.09 mA cm^{-1} of the ECSA, respectively. The ECSA for the MOR of the commercial Pt/C black was calculated as 0.1 mA cm^{-2} and used for comparison

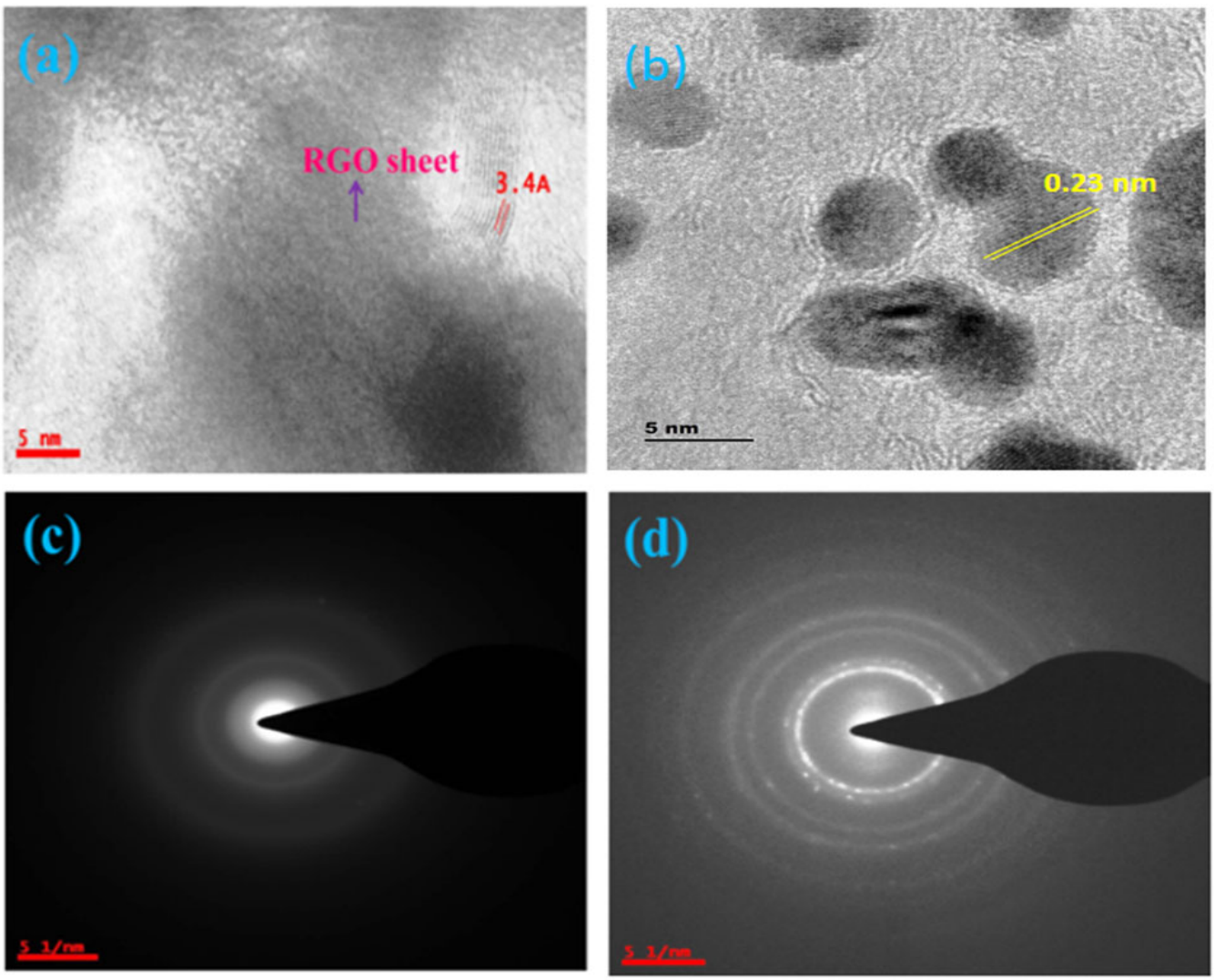

Fig. 8. HRTEM images of (a) rGO sheet and (b) Pt-Pd/rGO nanospheres. SAED pattern of (c) rGO sheet and (d) Pt-Pd/rGO nanospheres

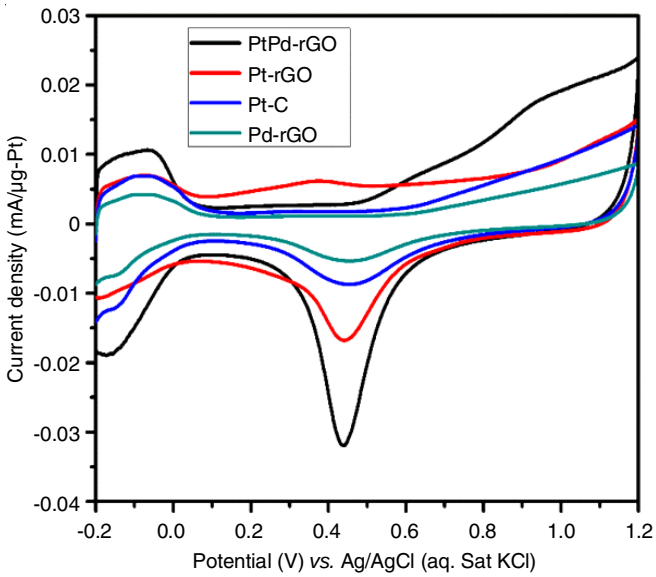

Fig. 9. Cyclic voltammograms (CVs) of Pt–Pd/rGO nanospheres; Pt/rGO; Pd-rGO; and commercial Pt/C catalysts recorded in 0.5 M H_2SO_4 solution at a scan rate of 50 mV s^{-1}

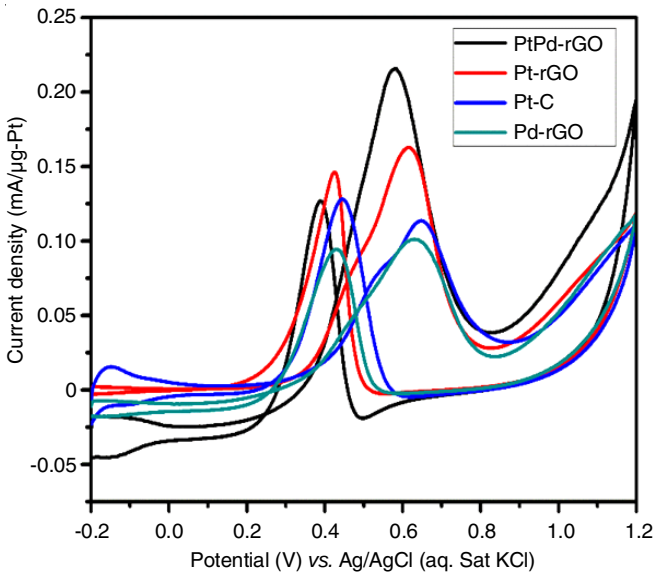

Fig. 10. Methanol oxidation cyclic voltammograms (CVs) of Pt-Pd/rGO; Pt/rGO; Pd-rGO; and commercial Pt/C catalysts recorded in 0.5 M H_2SO_4 + 1 M CH_3OH solution with a scan rate of 50 mV s^{-1}

purposes. The results indicate that the bimetallic Pt-Pd nanospheres supported on the rGO catalyst are approximately three times more active when exposed to MOR than the commercial Pt/C black catalyst. Furthermore, the mass activity of the electro-oxidation of the methanol on the bimetallic Pt-Pd/rGO nanocomposite was nearly two times greater (0.216 mA µg Pt^{-1}) than the commercial Pt/C black (0.11 mA µg Pt^{-1}). Therefore, the Pt-Pd/rGO nanocomposite shows excellent electrocatalytic performance owing to the smaller particle size, the dimensionality of the catalyst and the advantageously uniform distribution of particles on the rGO sheets. Electro-oxidation of methanol peaks is observed at approximately 0.6 V. This indicates that CO_2 (eqn. 1) and Pt (eqn. 2) adsorbed carbonaceous intermediates (mainly as CO) were formed. Therefore, the electrocatalytic activity could cease because of the adsorbed CO. The oxidation peaks during the backward scan can be related to the surplus oxidation of the adsorbed carbonaceous species to CO_2 (eqn. 3):

$$CH_3OH + H_2O \longrightarrow CO_2 + 6H^+ + 6e^- \quad (1)$$

$$Pt + CH_3OH \longrightarrow Pt\text{-}CO_{ads} + 4H^+ + 4e^- \quad (2)$$

$$Pt\text{-}CO_{ads} + H_2O \longrightarrow Pt + CO_2 + 2H^+ + 2e^- \quad (3)$$

The forward anodic (I_f) and backward cathodic peak current (I_b) ratios (I_f/I_b) can be used as an important index to estimate the electrocatalyst tolerance to CO accumulation. This ratio can also be used to explain the efficiencies of the electrocatalysts in the MOR. Generally, a greater I_f/I_b electrocatalysts value indicates a greater tolerance to intermediate carbonaceous species. The electrocatalysts I_f/I_b values of Pd/rGO, Pt/rGO, Pt/C and Pt-Pd/rGO of were observed at 1.46, 1.45, 1.47 and 1.52 respectively. The greater I_f/I_b value of Pt-Pd/rGO is an indication of a smaller accumulation of carbonaceous species and an increased methanol oxidation capability. The addition of Pd plays a vital role in increasing the activity of methanol. The size of the added Pd was similar to that of the Pt–Pd/rGOs catalysts (3-5 nm) and a commercial Pt/C black (3 nm). When comparing Pt to Pd, Pd has an uncommon exophilic nature and supports the oxidative elimination of CO on Pt. The nanometer size of Pd allows for the rapid oxidation of CO. Furthermore, by introducing Pd onto Pt it changes to enhance the adsorbed CO on platinum surface need to be converted to CO_2, which leads to the effortless weakening of the Pt-CO bonds. Therefore, simple CO elimination is expected. Furthermore, the tolerance of the electrocatalyst is increased because of the small amount of oxygen contained in the functional groups on the rGO.

Stability: Stability is an important characteristic of a high-quality electrocatalyst. Chronoamperometry curves demonstrate the stability of the materials in the MOR and it's measurements were performed in an electrolyte of 0.5 M H_2SO_4 + 1 M CH_3OH for 1000 s to understand the long-term performance of metals (Pt, Pd and Pt-Pd) supported on rGO catalysts for methanol electro-oxidation. Current-time plots of the electrocatalysts are shown in Fig. 11. The current densities of electrocatalysts were initially higher owing to a large number of active sites on the plane of the electrocatalyst. Pt-Pd/rGO nanospheres prepared using the wet reflux method shows excellent electrocatalytic activity for MOR and for retaining MOR current owing to the advantageous reaction conditions. Therefore, a Pt-Pd/rGO nanospheres is an effective alternative as an efficient electrocatalyst for direct methanol fuel cells (DMFCs).

Conclusion

A proficient wet chemical method demonstrated a simplified method to deposit bimetallic Pt-Pd nanospheres on rGO sheets using ascorbic acid as a reducing agent for the electro-oxidation of methanol. Methanol electro-oxidation on Pt-Pd / rGO can be significantly improved, as confirmed through CV measurements. The electrocatalyst activity of the prepared bimetallic Pt-Pd nanospheres supported on rGO sheets for MOR was higher and showed an excellent anti-CO contami-

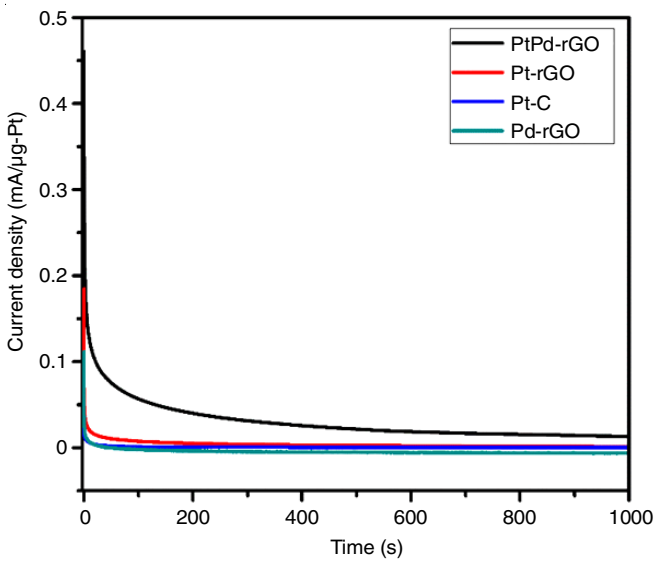

Fig. 11. Current-time curves of Pt-Pd/rGO nanospheres, Pt/rGO, Pd-rGO and commercial Pt/C catalysts measured in a 0.5 M H_2SO_4 + 1 M CH_3OH solution

nation property as compared with that of commercial Pt/C black. Pt-Pd nanospheres offer a uniform distribution, strong interaction on the rGO sheet and a high alloying degree. The optimized bimetallic Pt-Pd nanospheres anchored on the rGO sheets are a potential anode electrocatalyst for DMFC. Furthermore, this simple chemical preparation method can offer scope to develop other efficient nanocatalysts for fuel cells.

CONFLICT OF INTEREST

The authors declare that there is no conflict of interests regarding the publication of this article.

REFERENCES

1. E.G. Snyder, T.H. Watkins, P.A. Solomon, E.D. Thoma, R.W. Williams, G.S.W. Hagler, D. Shelow, D.A. Hindin, V.J. Kilaru and P.W. Preuss, *Environ. Sci. Technol.*, **47**, 11369 (2013); https://doi.org/10.1021/es4022602
2. J.C. Colmenares, R.F. Colmenares Quintero and I.S. Pieta, *Energy Technol.*, **4**, 881 (2016); https://doi.org/10.1002/ente.201600195
3. Z. Xiao, Y. Min, M. Liang, L. Liang, C.P. Liu, J.H. Liao and T. Lu, *Energy Environ. Sci.*, **4**, 201 (2011); https://doi.org/10.1039/C0EE00278J
4. S. Sun and Q. Gao, *Rare Met.*, **30(S1)**, 42 (2011); https://doi.org/10.1007/s12598-011-0234-4
5. L. Gao, W. Yue, S. Tao and L. Fan, *Langmuir*, **29**, 957 (2013); https://doi.org/10.1021/la303663x
6. X. Zhang, J. Zhu, C.S. Tiwary, Z. Ma, H. Huang, J. Zhang, Z. Lu, W. Huang and Y. Wu, *ACS Appl. Mater. Interfaces*, **8**, 10858 (2016); https://doi.org/10.1021/acsami.6b01580
7. S. Fu, C. Zhu, Q. Shi, D. Du and Y. Lin, *Catal. Sci. Technol.*, **6**, 5052 (2016); https://doi.org/10.1039/C5CY02288F
8. A. Morozan, B. Jousselme and S. Palacin, *Energy Environ. Sci.*, **4**, 1238 (2011); https://doi.org/10.1039/c0ee00601g
9. P. Pattanayak, N. Pramanik, P. Kumar and P.P. Kundu, *Int. J. Hydrogen Energy*, **43**, 11505 (2018); https://doi.org/10.1016/j.ijhydene.2017.04.300
10. Y. Liu, M. Chi, V. Mazumder, K.L. More, S. Soled, J. Henao and S. Sun, *Chem. Mater.*, **23**, 4199 (2011); https://doi.org/10.1021/cm2014785
11. W. Hong, J. Wang and E. Wang, *Nano Res.*, **8**, 2308 (2015); https://doi.org/10.1007/s12274-015-0741-y
12. W. Hong, Y. Liu, J. Wang and E. Wang, *J. Power Sources*, **241**, 751 (2013); https://doi.org/10.1016/j.jpowsour.2013.05.072
13. L.X. Ding, A.L. Wang, G.R. Li, Z.Q. Liu, W.X. Zhao, C.Y. Su and Y.X. Tong, *J. Am. Chem. Soc.*, **134**, 5730 (2012); https://doi.org/10.1021/ja212206m
14. A.C. Chen and P. Holt-Hindle, *Chem. Rev.*, **110**, 3767 (2010); https://doi.org/10.1021/cr9003902
15. Y.C. Lu, Z.C. Xu, H.A. Gasteiger, S. Chen, K. Hamad-Schifferli and Y. Shao-Horn, *J. Am. Chem. Soc.*, **132**, 12170 (2010); https://doi.org/10.1021/ja1036572
16. Y.Z. Lu and W. Chen, *Chem. Commun.*, **47**, 2541 (2011); https://doi.org/10.1039/C0CC04047A
17. J. Greeley, I.E. Stephens, A.S. Bondarenko, T.P. Johansson, H.A. Hansen, T.F. Jaramillo, J. Rossmeisl, I. Chorkendorff and J.K. Norskov, *Nat. Chem.*, **1**, 552 (2009); https://doi.org/10.1038/nchem.367
18. Y.Z. Zhang, Y.E. Gu, S.X. Lin, J.P. Wei, Z.H. Wang, C.M. Wang, Y. Du and W. Ye, *Electrochim. Acta*, **56**, 8746 (2011); https://doi.org/10.1016/j.electacta.2011.07.094
19. X. Zhong, Y.Y. Qin, X.L. Chen, W.L. Xu, G.L. Zhuang, X.N. Li and J. Wang, *Carbon*, **114**, 740 (2017); https://doi.org/10.1016/j.carbon.2016.12.004
20. S. Esabattina, V.R. Posa, H. Zhanglian, S. Godlaveeti, R.R. Nagi Reddy and A.R. Somala, *Int. J. Hydrogen Energy*, **43**, 4115 (2018); https://doi.org/10.1016/j.ijhydene.2017.07.193
21. J.P. Lai, R. Luque and G.B. Xu, *ChemCatChem*, **7**, 3206 (2015); https://doi.org/10.1002/cctc.201500471
22. E. Antolini, *Appl. Catal. B*, **123-124**, 52 (2012); https://doi.org/10.1016/j.apcatb.2012.04.022
23. C. Hou, M. Zhang, A. Halder and Q. Chi, *Electrochim. Acta*, **242**, 202 (2017); https://doi.org/10.1016/j.electacta.2017.04.117
24. Y. Yang, L.M. Luo, T.F. Guo, Z.X. Dai, R.H. Zhang, C.H. Sun and X.W. Zhou, *J. Electroanal. Chem.*, **783**, 132 (2016); https://doi.org/10.1016/j.jelechem.2016.11.034
25. L. Sun, H. Wang, K. Eid, S.M. Alshehri, V. Malgras, Y. Yamauchi and L. Wang, *Electrochim. Acta*, **188**, 845 (2016); https://doi.org/10.1016/j.electacta.2015.12.068
26. X. Zhang, G. Wu, Z. Cai and X. Chen, *Talanta*, **134**, 132 (2015); https://doi.org/10.1016/j.talanta.2014.11.002
27. S. Du, Y. Lu and R. Steinberger-Wilckens, *Carbon*, **79**, 346 (2014); https://doi.org/10.1016/j.carbon.2014.07.076
28. J.X. Feng, Q.L. Zhang, A.J. Wang, J. Wei, J.R. Chen and J.J. Feng, *Electrochim. Acta*, **142**, 343 (2014); https://doi.org/10.1016/j.electacta.2014.07.152
29. L. Zhang, X.F. Zhang, X.L. Chen, A.J. Wang, D.M. Han, Z.G. Wang and J.J. Feng, *J. Colloid Interface Sci.*, **536**, 556 (2019); https://doi.org/10.1016/j.jcis.2018.10.080
30. V.R. Posa, V. Annavaram, J.R. Koduru, V.R. Ammireddy and A.R. Somala, *Korean J. Chem. Eng.*, **33**, 456 (2016); https://doi.org/10.1007/s11814-015-0145-4
31. K. Wu, Q. Zhang, D. Sun, X. Zhu, Y. Chen, T. Lu and Y. Tang, *Int. J. Hydrogen Energy*, **40**, 6530 (2015); https://doi.org/10.1016/j.ijhydene.2015.03.115
32. H. Zhang, X. Xu, P. Gu, C. Li, P. Wu and C. Cai, *Electrochim. Acta*, **56**, 7064 (2011); https://doi.org/10.1016/j.electacta.2011.05.118
33. W. Qian, R. Hao, J. Zhou, M. Eastman, B.A. Manhat, Q. Sun, A.M. Goforth and J. Jiao, *Carbon*, **52**, 595 (2013); https://doi.org/10.1016/j.carbon.2012.10.031
34. T.V. Cuong, V.H. Pham, Q.T. Tran, S.H. Hahn, J.S. Chung, E.W. Shin and E.J. Kim, *Mater. Lett.*, **64**, 399 (2010); https://doi.org/10.1016/j.matlet.2009.11.029
35. C.L. Lee, H.P. Chiou, S.C. Wu and C.C. Wu, *Electrochim. Acta*, **56**, 687 (2010); https://doi.org/10.1016/j.electacta.2010.09.096